Beam Modeling in a Floating Frame of Reference for Torsion Dynamics of Helicopter Rotor Blades

Felix Weiss, Joshua Merlis

German Aerospace Center (DLR)
Institute of Flight Systems
Lilienthalplatz 7, 38108 Braunschweig, Germany
felix.weiss@dlr.de

ABSTRACT

In the ongoing development of DLR's Versatile Aeromechanics Simulation Tool, an elastic beam model is integrated into the multibody system based on the floating frame of reference formulation. Although the application of this formulation for one dimensional beam models has already been addressed in the literature, the challenge remains to properly model the torsion dynamics of rotor blades — especially under high centrifugal loads. To this aim, this work suggests the consideration of rotational shape functions in the inertia shape integrals and in the application of gravitational, inertial, and external loads. This modified approach is validated based on the structural analysis of a rotor blade with complex geometrical properties.

Keywords: Torsion Dynamics, Inertia Shape Integrals, Centrifugal Loads, Rotational Shape Functions, Propeller Moment.

1 INTRODUCTION

Helicopter rotor blades are usually slender structures with a rotor radius much larger than the chord length and thickness. This geometrical property encourages modeling the blade as a one dimensional (1D) beam, which saves computational costs compared to a 3D structural model. For this reason, multi-physics tools for helicopter (rotor) simulations — so-called comprehensive codes — commonly employ beam models to simulate the blades. This approach is also taken in the Versatile Aeromechanics Simulation Tool (VAST) [1].

VAST's multibody system (MBS) includes both rigid and flexible bodies. For flexible bodies, the nodal position states $\mathbf{r}_\mathrm{I}$ and velocity states $\mathbf{r}_\mathrm{II} = \dot{\mathbf{r}}_\mathrm{I}$ of the finite element (FE) model describe the body deformation with respect to the floating frame of reference (FFR) [2], which moves ("floats") relative to the inertial frame by the linear and angular velocities $\mathbf{v}$ and ω. In this work, the vectors $\mathbf{v}$ and ω are expressed in the coordinates of the FFR. These vectors represent the rigid body portion of motion with the corresponding mass matrix $\mathbf{m}_\mathrm{RR}$, inertia tensor $\bar{\mathbf{J}}_{\theta\theta}$, and coupling matrix $\tilde{\bar{\mathbf{S}}}_\mathrm{t}^\mathrm{T}$, see the upper part of equation 1:

$$\begin{bmatrix} \mathbf{m}_\mathrm{RR} & \tilde{\bar{\mathbf{S}}}_\mathrm{t}^\mathrm{T} & \mathbf{0} & \bar{\mathbf{S}} \\ & \bar{\mathbf{J}}_{\theta\theta} & \mathbf{0} & \bar{\mathbf{J}}_{\theta\mathrm{f}} \\ & & \mathbf{I} & \mathbf{0} \\ sym. & & & \mathbf{M}_\mathrm{ff} \end{bmatrix} \begin{bmatrix} \dot{\mathbf{v}} \\ \dot{\omega} \\ \dot{\mathbf{r}}_\mathrm{I} \\ \dot{\mathbf{r}}_\mathrm{II} \end{bmatrix} = \begin{bmatrix} \mathbf{0} & \mathbf{0} & \mathbf{0} & \mathbf{0} \\ \mathbf{0} & \mathbf{0} & \mathbf{0} & \mathbf{0} \\ \mathbf{0} & \mathbf{0} & \mathbf{0} & \mathbf{I} \\ \mathbf{0} & \mathbf{0} & -\mathbf{K}_\mathrm{ff} & -\mathbf{D}_\mathrm{ff} \end{bmatrix} \begin{bmatrix} \mathbf{v} \\ \omega \\ \mathbf{r}_\mathrm{I} \\ \mathbf{r}_\mathrm{II} \end{bmatrix} + \begin{bmatrix} \mathbf{Q}_\mathrm{g}^\mathrm{R} \\ \mathbf{Q}_\mathrm{g}^\theta \\ \mathbf{0} \\ \mathbf{Q}_\mathrm{g}^\mathrm{f} \end{bmatrix} + \begin{bmatrix} \mathbf{Q}_\mathrm{v}^\mathrm{R} \\ \mathbf{Q}_\mathrm{v}^\theta \\ \mathbf{0} \\ \mathbf{Q}_\mathrm{v}^\mathrm{f} \end{bmatrix} + \begin{bmatrix} \mathbf{Q}_\mathrm{e}^\mathrm{R} \\ \mathbf{Q}_\mathrm{e}^\theta \\ \mathbf{0} \\ \mathbf{Q}_\mathrm{e}^\mathrm{f} \end{bmatrix} \quad (1)$$

The second order differential equation of the FE system has been converted to first order form (lower part of equation 1), in which the FE system's mass $\mathbf{M}_\mathrm{ff}$, stiffness $\mathbf{K}_\mathrm{ff}$, and damping $\mathbf{D}_\mathrm{ff}$ matrices are found. $\mathbf{K}_\mathrm{ff}$ is composed of both the structural and geometric stiffnesses. $\mathbf{D}_\mathrm{ff}$ depends on the structural damping model. In this paper, no structural damping is applied, i.e. $\mathbf{D}_\mathrm{ff} = \mathbf{0}$. The rightmost entries $\bar{\mathbf{S}}$ and $\bar{\mathbf{J}}_{\theta\mathrm{f}}$ in the upper part of the overall mass matrix constitute coupling terms between the rigid body motion and the flexible motion. The right hand side includes gravitational loads $\mathbf{Q}_\mathrm{g}$, inertial loads $\mathbf{Q}_\mathrm{v}$, and external loads $\mathbf{Q}_\mathrm{e}$ acting on the rigid translatory, rigid rotational, and flexible motion (superscripts R, θ, and f, respectively).

The set of nodal states $(\mathbf{r}_I, \mathbf{r}_{II})$, the assembly of $\mathbf{K}_{\mathrm{ff}}$, as well as a predominant portion of the shape functions that are referenced in the following are based on the Beam Advanced Model (BAM) [3, 4]. BAM is specialized to address the needs of helicopter blade modeling. Through the introduction of differential degrees of freedom,[1] it enables the efficient computation of discontinuous physical characteristics, without the need for a refined discretization. BAM's shape functions are derived based on third-order Hermite polynomials, and are provided in the literature for all three translatory deformations and torsion about the beam's axis. Rotations about the cross sectional axes are then computed based on the Timoshenko formulation.

According to the general theory [2, 5], several submatrices and vectors of equation 1 include volume integrals with both the mass density $\rho(x,y,z)$ and the translatory shape function matrix $\mathbf{S}_{\mathrm{tra}}(x,y,z)$ as integrands—the so-called inertia shape integrals. x, y, and z are the coodinates of the volume increment with respect to the FFR. The shape functions are also used to evaluate the kinematics of the system. For example, a particle's translatory velocity reads $\dot{\bar{\mathbf{u}}} = \mathbf{S}_{\mathrm{tra}}(x,y,z)\,\mathbf{r}_{II}$ in the general 3D formulation. The bar indicates that the quantity is given relative to the FFR. In contrast, for a 1D beam with torsional degrees of freedom as shown in Figure 1, $\mathbf{S}_{\mathrm{tra}}(\zeta)$ is insufficient to evaluate the kinematics of a particle that is located at a distance from the reference axis. ζ
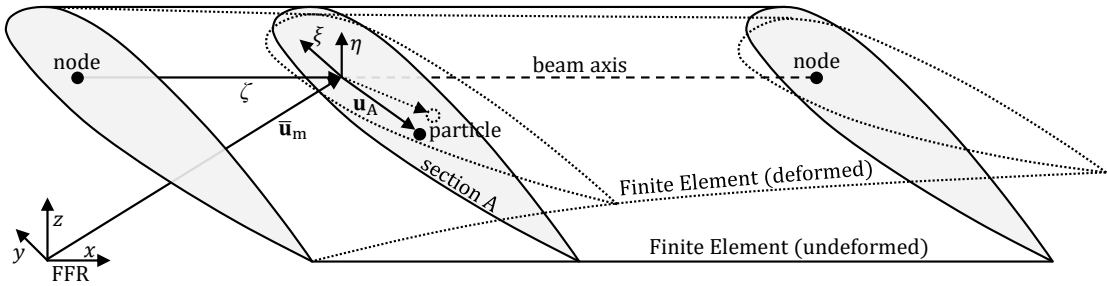

Figure 1. Particle in a cross section A moving due to torsional deformation of a 1D beam

is the coordinate along this axis, and $\mathbf{u}_A$ is the particle's offset from the reference axis within the cross section. The particle's velocity is $\dot{\bar{\mathbf{u}}} = \mathbf{S}_{\mathrm{tra}}(\zeta)\,\mathbf{r}_{II} + \omega_{\mathrm{flex}} \times \mathbf{u}_A$ with $\omega_{\mathrm{flex}} = \mathbf{S}_{\mathrm{rot}}(\zeta)\,\mathbf{r}_{II}$. Here, the rotational shape function matrix $\mathbf{S}_{\mathrm{rot}}$ has been introduced, as presented in [6]. For a consistent consideration of $\mathbf{S}_{\mathrm{rot}}$ in equation 1, this paper proposes the usage of the complemented shape function matrix

$$\mathbf{S}(\zeta,\xi,\eta) = \mathbf{S}_{\mathrm{tra}}(\zeta) - \tilde{\mathbf{u}}_A(\xi,\eta)\mathbf{S}_{\mathrm{rot}}(\zeta), \tag{2}$$

where (ξ,η) are the coordinates within the cross section and the tilde symbol denotes the cross product operator according to

$$\mathbf{a} \times \mathbf{b} = \begin{bmatrix} a_2 b_3 - a_3 b_2 \\ a_3 b_1 - a_1 b_3 \\ a_1 b_2 - a_2 b_1 \end{bmatrix} = \tilde{\mathbf{a}}\mathbf{b} = \begin{bmatrix} 0 & -a_3 & a_2 \\ a_3 & 0 & -a_1 \\ -a_2 & a_1 & 0 \end{bmatrix} \begin{bmatrix} b_1 \\ b_2 \\ b_3 \end{bmatrix}. \tag{3}$$

The expression $\dot{\bar{\mathbf{u}}} = \mathbf{S}(\zeta,\xi,\eta)\,\mathbf{r}_{II}$ evaluates to the same terms as given above. In section 2, the individual terms of equation 1 are given based on the complemented shape function matrix according to equation 2. The benefit of the modified implementation in the analysis of rotating beams (especially helicopter rotor blades) is presented in section 3.

---

[1]Included are the derivatives with respect to the beam's length axis of the axial elongation and torsion about this axis, at locations immediately to each side of the node.

2 THEORY

The terms of equation 1 are taken from the literature [2, 5] in their general 3D formulation. This section presents two modifications of the terms:

- The 3D volume integrals are transformed to 1D integrals along the beam's length. The pre-evaluated cross-sectional integrals, which are included in the beam model's configuration data, appear as integrands. This transformation improves performance and facilitates the configuration of beam models.

- The complemented shape function matrix $\mathbf{S} = \mathbf{S}_{\text{tra}} - \tilde{\mathbf{u}}_A \mathbf{S}_{\text{rot}}$ is consistently applied.

2.1 Cross sectional mass moments in the local frame

First, the following cross sectional integrals are defined. In the local cross section frame, the offset $\mathbf{u}_A^{\text{loc}}$ of a particle from the cross section reference (beam axis intersection point) reads $\mathbf{u}_A^{\text{loc}} = (0, \xi, \eta)^{\text{T}}$. Table 1 lists the cross sectional mass moments in the local frame. These are included in the beam model's configuration data and do not depend on deformation, so they can be evaluated in advance.

Table 1. cross sectional mass moments, integrated in the local cross sectional frame

0th order	$I_{00} = \int_A \rho \, dA$		
1st order	$I_{10} = \int_A \rho \, \xi \, dA$	$I_{01} = \int_A \rho \, \eta \, dA$	
2nd order	$I_{20} = \int_A \rho \, \xi^2 \, dA$	$I_{02} = \int_A \rho \, \eta^2 \, dA$	$I_{11} = \int_A \rho \, \xi \, \eta \, dA$

2.2 Cross sectional mass moments in the FFR

The transformation matrix $\mathbf{T}$ rotates vectors and matrices from the FFR to the local cross sectional frame. Thus the application of $\mathbf{T}^{\text{T}}\mathbf{v}$ for vectors $\mathbf{v}$ and $\mathbf{T}^{\text{T}}\mathbf{M}\mathbf{T}$ for matrices $\mathbf{M}$ rotates from the local frame to the FFR. The FFR-transformed vectors and matrices are:

$$\int_A \rho \, dA = I_{00} \tag{4}$$

$$\int_A \rho \mathbf{u}_A \, dA = \mathbf{T}^{\text{T}} \begin{bmatrix} 0 \\ I_{10} \\ I_{01} \end{bmatrix} \quad \text{or} \quad \int_A \rho \tilde{\mathbf{u}}_A \, dA = \mathbf{T}^{\text{T}} \begin{bmatrix} 0 & -I_{01} & I_{10} \\ I_{01} & 0 & 0 \\ -I_{10} & 0 & 0 \end{bmatrix} \mathbf{T} \tag{5}$$

$$\int_A \rho \tilde{\mathbf{u}}_A^{\text{T}} \tilde{\mathbf{u}}_A \, dA = \mathbf{T}^{\text{T}} \begin{bmatrix} I_{20}+I_{02} & 0 & 0 \\ 0 & I_{02} & -I_{11} \\ 0 & -I_{11} & I_{20} \end{bmatrix} \mathbf{T} \tag{6}$$

$$\int_A \rho \mathbf{u}_A \mathbf{u}_A^{\text{T}} \, dA = \mathbf{T}^{\text{T}} \begin{bmatrix} 0 & 0 & 0 \\ 0 & I_{20} & I_{11} \\ 0 & I_{11} & I_{02} \end{bmatrix} \mathbf{T} \tag{7}$$

$\mathbf{T}$ includes two rotations:

1. The orientation of the local frame with respect to the FFR in the undeformed configuration. This contribution can be large, e.g. when the beam axis is bent, as is the case for some modern helicopter rotor blades like the one investigated in section 3.2.

2. The flexible rotation due to deformation of the beam. This part is usually small but can be important — especially for the torsional dynamics, as presented in section 3.1.

Consequently, the deformation states $\mathbf{r}_I$ affect the rotation matrix $\mathbf{T}$ in equations 5 – 7, so that these integrals — when expressed in the FFR — depend on the deformation of the beam as well.

2.3 Inertia shape integrals

The particle's location relative to the FFR is $\bar{\mathbf{u}} = \bar{\mathbf{u}}_m + \mathbf{u}_A$, where $\bar{\mathbf{u}}_m$ is the cross section reference location (affected by translatory flexible displacements), and $\mathbf{u}_A$ is the offset within the cross section (affected by rotational flexible displacements). This composition is used in the following for the transformation of the 3D integrals over the volume V to 1D integrals along the beam axis ζ. The integrals over the cross-sectional area A (equations $4-7$) are shown in red to make them more easily recognizable. The integrals corresponding to rigid body motion (not affected by the introduction of the complemented shape function matrix) are:

$$\mathbf{m}_{RR} = \int_V \rho\,\mathbf{I}\,dV = \mathbf{I}\int_\zeta \int_A \rho\,dA\,d\zeta \tag{8}$$

$$\bar{\mathbf{S}}_t = \int_V \rho\,\bar{\mathbf{u}}\,dV = \int_\zeta \int_A \rho\,(\bar{\mathbf{u}}_m + \mathbf{u}_A)\,dA\,d\zeta = \int_\zeta \left[\bar{\mathbf{u}}_m \int_A \rho\,dA + \int_A \rho\,\mathbf{u}_A\,dA\right]d\zeta \tag{9}$$

$$\bar{\mathbf{J}}_{\theta\theta} = \int_V \rho\,\tilde{\bar{\mathbf{u}}}^T\tilde{\bar{\mathbf{u}}}\,dV = \int_\zeta \int_A \rho\,\widetilde{(\bar{\mathbf{u}}_m + \mathbf{u}_A)}^T\,\widetilde{(\bar{\mathbf{u}}_m + \mathbf{u}_A)}\,dA\,d\zeta$$

$$= \int_\zeta \left[\tilde{\bar{\mathbf{u}}}_m^T \tilde{\bar{\mathbf{u}}}_m \int_A \rho\,dA + \tilde{\bar{\mathbf{u}}}_m^T \int_A \rho\,\tilde{\mathbf{u}}_A\,dA + \int_A \rho\,\tilde{\mathbf{u}}_A^T\,dA\,\tilde{\bar{\mathbf{u}}}_m + \int_A \rho\,\tilde{\mathbf{u}}_A^T\,\tilde{\mathbf{u}}_A\,dA\right]d\zeta \tag{10}$$

The integrals related to flexible motion are based on the complemented shape function matrix $\mathbf{S}$ according to equation 2. These are:

$$\bar{\mathbf{S}} = \int_V \rho\,\mathbf{S}\,dV = \int_\zeta \int_A \rho\,(\mathbf{S}_{tra} - \tilde{\mathbf{u}}_A\,\mathbf{S}_{rot})\,dA\,d\zeta = \int_\zeta \left[\mathbf{S}_{tra} \int_A \rho\,dA - \int_A \rho\,\tilde{\mathbf{u}}_A\,dA\,\mathbf{S}_{rot}\right]d\zeta \tag{11}$$

$$\bar{\mathbf{J}}_{\theta f} = \int_V \rho\,\tilde{\bar{\mathbf{u}}}\,\mathbf{S}\,dV = \int_\zeta \int_A \rho\,\left(\widetilde{\bar{\mathbf{u}}_m + \mathbf{u}_A}\right)(\mathbf{S}_{tra} - \tilde{\mathbf{u}}_A\,\mathbf{S}_{rot})\,dA\,d\zeta$$

$$= \int_\zeta \left[\left(\tilde{\bar{\mathbf{u}}}_m \int_A \rho\,dA + \int_A \rho\,\tilde{\mathbf{u}}_A\,dA\right)\mathbf{S}_{tra}\right.$$

$$\left. - \left(\tilde{\bar{\mathbf{u}}}_m \int_A \rho\,\tilde{\mathbf{u}}_A\,dA - \int_A \rho\,\tilde{\mathbf{u}}_A^T\,\tilde{\mathbf{u}}_A\,dA\right)\mathbf{S}_{rot}\right]d\zeta \tag{12}$$

$$\mathbf{M}_{ff} = \int_V \rho\,\mathbf{S}^T\mathbf{S}\,dV = \int_\zeta \int_A \rho\,(\mathbf{S}_{tra} - \tilde{\mathbf{u}}_A\mathbf{S}_{rot})^T(\mathbf{S}_{tra} - \tilde{\mathbf{u}}_A\mathbf{S}_{rot})\,dA\,d\zeta$$

$$= \int_\zeta \left[\mathbf{S}_{tra}^T\mathbf{S}_{tra} \int_A \rho\,dA - \mathbf{S}_{tra}^T \int_A \rho\,\tilde{\mathbf{u}}_A\,dA\,\mathbf{S}_{rot}\right.$$

$$\left. - \mathbf{S}_{rot}^T\left(\int_A \rho\,\tilde{\mathbf{u}}_A\,dA\right)^T\mathbf{S}_{tra} + \mathbf{S}_{rot}^T \int_A \rho\,\tilde{\mathbf{u}}_A^T\,\tilde{\mathbf{u}}_A\,dA\,\mathbf{S}_{rot}\right]d\zeta \tag{13}$$

Note that $\mathbf{S}_{tra} = \mathbf{S}_{tra}(\zeta)$ and $\mathbf{S}_{rot} = \mathbf{S}_{rot}(\zeta)$. Along with the cross sectional integrals' dependency on the deformation state $\mathbf{r}_I$ due to flexible rotation (cf. section 2.2), the integrals in equations 9, 10, and 12 also depend on the deformation because $\bar{\mathbf{u}}_m = \bar{\mathbf{u}}_m(\zeta, \mathbf{r}_I)$.

2.4 Load terms

Finally, the loads $\mathbf{Q}_g^f$, $\mathbf{Q}_v^f$, and $\mathbf{Q}_e^f$ also contain the shape function matrix $\mathbf{S}$. $\mathbf{g}$ denotes the gravitational acceleration expressed in the FFR, while $\mathbf{a}$ is the FFR acceleration due to angular velocities in the MBS.

$$\mathbf{Q}_g^f = \int_V \rho\, \mathbf{S}^T \mathbf{g}\, dV = \bar{\mathbf{S}}^T \mathbf{g} \tag{14}$$

$$
\begin{aligned}
\mathbf{Q}_v^f &= -\int_V \rho\, \mathbf{S}^T \left(\mathbf{a} + \tilde{\omega}\tilde{\omega}\bar{\mathbf{u}} + 2\tilde{\omega}\dot{\mathbf{u}}\right) dV \\
&= -\int_\zeta \int_A \rho\, \left(\mathbf{S}_{\text{tra}} - \tilde{\mathbf{u}}_A \mathbf{S}_{\text{rot}}\right)^T \left(\mathbf{a} + \tilde{\omega}\tilde{\omega}\left(\bar{\mathbf{u}}_m + \mathbf{u}_A\right) + 2\tilde{\omega}\left(\mathbf{S}_{\text{tra}} - \tilde{\mathbf{u}}_A \mathbf{S}_{\text{rot}}\right)\mathbf{r}_{\text{II}}\right) dA\, d\zeta \\
&= \int_\zeta \Bigg[\mathbf{S}_{\text{tra}}^T \left(\left(-\mathbf{a} - \tilde{\omega}\tilde{\omega}\bar{\mathbf{u}}_m - 2\tilde{\omega}\mathbf{S}_{\text{tra}}\mathbf{r}_{\text{II}}\right)\int_A \rho\, dA - \tilde{\omega}\tilde{\omega}\int_A \rho\mathbf{u}_A dA + 2\tilde{\omega}\int_A \rho\tilde{\mathbf{u}}_A dA\, \mathbf{S}_{\text{rot}}\mathbf{r}_{\text{II}} \right) \\
&\qquad + \mathbf{S}_{\text{rot}}^T \left(\int_A \rho\tilde{\mathbf{u}}_A^T dA\left(\mathbf{a} + \tilde{\omega}\tilde{\omega}\bar{\mathbf{u}}_m + 2\tilde{\omega}\mathbf{S}_{\text{tra}}\mathbf{r}_{\text{II}}\right) - \tilde{\omega}\int_A \rho\tilde{\mathbf{u}}_A^T \tilde{\mathbf{u}}_A\, dA\, \omega \right. \\
&\qquad \left. + 2\left(\tilde{\omega}\int_A \rho\mathbf{u}_A \mathbf{u}_A^T\, dA - \int_A \rho\tilde{\mathbf{u}}_A^T \tilde{\mathbf{u}}_A\, dA\, \tilde{\omega}\right)\mathbf{S}_{\text{rot}}\mathbf{r}_{\text{II}} \right) \Bigg] d\zeta
\end{aligned} \tag{15}
$$

$$\mathbf{Q}_e^f = \sum_{i=1}^n \mathbf{S}_{\text{tra}}^T(\zeta_i)\mathbf{F}_i + \mathbf{S}_{\text{rot}}^T(\zeta_i)\mathbf{M}_i \tag{16}$$

In equation 15, the conversions $\tilde{\mathbf{u}}_A^T \tilde{\omega}\tilde{\omega}\mathbf{u}_A = -\tilde{\omega}\tilde{\mathbf{u}}_A^T \tilde{\mathbf{u}}_A \omega$ and $-\tilde{\mathbf{u}}_A^T \tilde{\omega}\tilde{\mathbf{u}}_A = \tilde{\omega}\mathbf{u}_A \mathbf{u}_A^T - \tilde{\mathbf{u}}_A^T \tilde{\mathbf{u}}_A \tilde{\omega}$ have been used. Equation 16 differs from the other load terms because the external loads $\mathbf{Q}_e^f$ are n pairs of discrete forces and moments $(\mathbf{F}_i, \mathbf{M}_i)$, while $\mathbf{Q}_g^f$ and $\mathbf{Q}_v^f$ are volume forces.

3 RESULTS

The modified implementation has a significant influence on the inertial loads term $\mathbf{Q}_v^f$ acting on the flexible motion. The added value of using the complemented shape function matrix $\mathbf{S} = \mathbf{S}_{\text{tra}} - \tilde{\mathbf{u}}_A \mathbf{S}_{\text{rot}}$ instead of the original shape function matrix $\mathbf{S} = \mathbf{S}_{\text{tra}}$ for calculating $\mathbf{Q}_v^f$ is illustrated in the following. Section 3.1 verifies the implementation based on an academic test case with analytic reference results, and section 3.2 presents results for a practical test case.

3.1 Verification based on an academic test case

The modified implementation including $\mathbf{S}_{\text{rot}}$ accounts for the effect of inertial loads on the beam's nodes' flexible rotation. One particularly relevant effect of inertial loads on flexible rotation in helicopter rotor analysis is the propeller moment [7, 8], which is illustrated in Figure 2. The cross
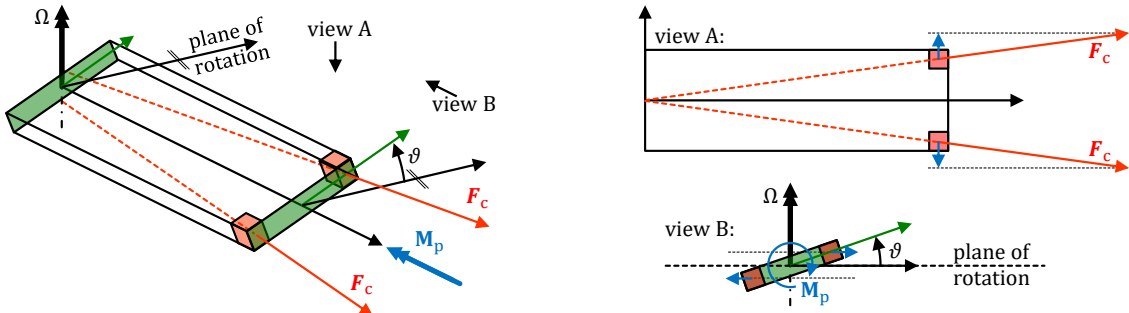

Figure 2. Phenomenological explanation of the propeller moment $\mathbf{M}_p$

section of a 1D-beam may have different inertial properties in its two directions. For example, the lead-lag inertia per unit length of a typical rotor blade cross section is larger than its flap inertia per unit length. In this case, for a rotating blade, the centrifugal forces $\mathbf{F}_c$ generate the propeller moment $\mathbf{M}_p$ which tends to rotate the section such that it lays flat in the plane of rotation.

The configuration used to verify the propeller moment is sketched in Figure 3. The "beam" consists of four quasi-massless and torsionally compliant FE elements (grey part of the beam), which together have the torsional stiffness k. The fifth and last element is a quasi-rigid cuboid of size $a \cdot a \cdot c$ with homogeneous mass density ρ (blue part of the beam). Note that the beam axis ζ is not bent, i.e. the cuboid's longitudinal axis coincides with one of its shorter dimensions a and not with the longer side c. The beam is clamped to a hub with a constant rotational speed Ω and has an undeformed inclination of ϑ_{pre}. Due to the propeller moment acting on the cuboid, the beam is elastically twisted by $\vartheta_{\mathrm{flex}} < 0$.

$$\Omega = 100\,\mathrm{rad/s}$$
$$\vartheta_{\mathrm{pre}} = 1^\circ$$
$$k = 2750\,\mathrm{Nm/rad}$$
$$R = 10\,\mathrm{m}$$
$$a = 0.1\,\mathrm{m}$$
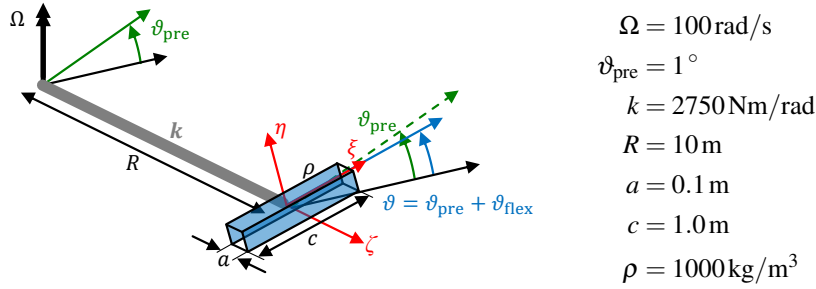$$c = 1.0\,\mathrm{m}$$
$$\rho = 1000\,\mathrm{kg/m^3}$$

Figure 3. Beam configuration for verifying the propeller moment

The propeller moment acting on the cuboid with inclination $\vartheta = \vartheta_{\mathrm{pre}} + \vartheta_{\mathrm{flex}}$ is

$$M_{\mathrm{p}} = -\Omega^2 \cdot \left(I_{\eta\eta} - I_{\xi\xi}\right) \cdot \sin(\vartheta) \cdot \cos(\vartheta), \tag{17}$$

where the mass moments of inertia are $I_{\eta\eta} = m/12\left(a^2 + c^2\right)$ and $I_{\xi\xi} = m/12\left(a^2 + a^2\right)$ with $m = \rho\,a^2\,c$. The expression given in equation 17 can, for example, be identified in the torsional differential equation presented in [9] and is explicitly called "propeller moment" in [8]. The torsional stiffness of the rotating beam in equilibrium counteracts the propeller moment, i.e. $\vartheta_{\mathrm{flex}} = M_{\mathrm{p}}/k$. Since $\vartheta < 1^\circ$, the simplifications $\sin(\vartheta) \approx \vartheta$ and $\cos(\vartheta) \approx 1$ are justifiable so that

$$\vartheta_{\mathrm{flex}} = \frac{-\Omega^2}{k}\left(I_{\eta\eta} - I_{\xi\xi}\right) \cdot \left(\vartheta_{\mathrm{pre}} + \vartheta_{\mathrm{flex}}\right) \Leftrightarrow \vartheta_{\mathrm{flex}} = \frac{\frac{-\Omega^2}{k}\left(I_{\eta\eta} - I_{\xi\xi}\right)\vartheta_{\mathrm{pre}}}{1 + \frac{\Omega^2}{k}\left(I_{\eta\eta} - I_{\xi\xi}\right)} = -0.75^\circ. \tag{18}$$

In VAST, an equilibrium calculation is performed for this configuration, modeling the beam with BAM elements. Table 2 compares the resulting flexible tip twist for $\mathbf{S} = \mathbf{S}_{\mathrm{tra}}$ and $\mathbf{S} = \mathbf{S}_{\mathrm{tra}} - \tilde{\mathbf{u}}_A\,\mathbf{S}_{\mathrm{rot}}$ with the analytical solution. As expected, $\mathbf{S}_{\mathrm{tra}}$ does not account for the effect at all. However, with $\mathbf{S} = \mathbf{S}_{\mathrm{tra}} - \tilde{\mathbf{u}}_A\,\mathbf{S}_{\mathrm{rot}}$, the result is correct within the accuracy expected from the numerics and discretization.

Table 2. Equilibrium flexible twist $\vartheta_{\mathrm{flex}}$ of the beam in Figure 3

Analytical	VAST-BAM, $\mathbf{S} = \mathbf{S}_{\mathrm{tra}}$	VAST-BAM, $\mathbf{S} = \mathbf{S}_{\mathrm{tra}} - \tilde{\mathbf{u}}_A\,\mathbf{S}_{\mathrm{rot}}$
$\vartheta_{\mathrm{flex}} = -0.75^\circ$	$\vartheta_{\mathrm{flex}} = 0^\circ$	$\vartheta_{\mathrm{flex}} = -0.74^\circ$

To address the frequency-domain behavior of the beam, the restoring propeller moment can be interpreted as an additional stiffness k_{p}, for which the small angle assumption for ϑ is again applied:

$$k_{\mathrm{p}} = \partial M_{\mathrm{p}}/\partial\vartheta = \Omega^2\left(I_{\eta\eta} - I_{\xi\xi}\right) \tag{19}$$

The expected torsional eigenfrequency is $\sqrt{(k+k_{\mathrm{p}})/I_{\zeta\zeta}}$ with $I_{\zeta\zeta} = m/12\,(c^2+a^2)$. Table 3 presents the first torsion eigenfrequency of the beam for the non-rotating case $\Omega = 0\,\mathrm{rad/s}$ and for $\Omega = 100\,\mathrm{rad/s}$. In the non-rotating case, all results are identical, confirming the consistency of the analytical and computational structural models (without inertial loads). At $\Omega = 100\,\mathrm{rad/s}$, a first torsional eigenfrequency of 18.19 Hz is expected analytically. However, with $\mathbf{S} = \mathbf{S}_{\mathrm{tra}}$, only a slight increase in eigenfrequency is observed compared to the non-rotating case. This is attributed to geometric stiffening effects, which are *not* considered in the analytical calculation. With $\mathbf{S} = \mathbf{S}_{\mathrm{tra}} - \tilde{\mathbf{u}}_{\mathrm{A}}\,\mathbf{S}_{\mathrm{rot}}$, the eigenfrequency prediction of 18.33 Hz is only slightly higher than the analytical reference ($+1\%$), which again is explained by geometric stiffening.

Table 3. First torsion eigenfrequency of the beam in Figure 3, also with $\Omega = 0\,\mathrm{rad/s}$

Ω	0 rad/s	100 rad/s
Analytical	9.10 Hz	18.19 Hz
VAST-BAM, $\mathbf{S} = \mathbf{S}_{\mathrm{tra}}$	9.10 Hz	9.37 Hz
VAST-BAM, $\mathbf{S} = \mathbf{S}_{\mathrm{tra}} - \tilde{\mathbf{u}}_{\mathrm{A}}\,\mathbf{S}_{\mathrm{rot}}$	9.10 Hz	18.33 Hz

These results show that the complemented shape function matrix is needed to account for the propeller moment. Note that the rotation of the cross sectional integrals in equations $5 - 7$ by $\mathbf{T}$ *must* include the deformation, i.e. $\mathbf{T} = \mathbf{T}(\mathbf{r}_{\mathrm{I}})$. This is crucial to determine k_{p} (see equation 19) because M_{p} depends on $\vartheta_{\mathrm{flex}}$. The torsion eigenfrequency, in turn, depends on k_{p}.

3.2 Validation based on a practical test case

As an example of a modern rotor blade, a prototype blade [3] from a helicopter rotor research program at Airbus is investigated. Figure 4 shows the blade with a double-swept planform. The

Figure 4. Double-swept prototype blade, picture from [3]

real blade is attached to the rotor hub via a combined bearing which allows flap (out of plane) and lead-lag (in plane) motion of the blade, and features an elastomeric spring-damper device. Furthermore, a dedicated lead-lag damper is integrated into the blade root. The kinematics of this lead-lag damper along with the blade pitch actuation via control rods constitute multiple load paths, which are not yet supported in VAST. Therefore, a simplified blade attachment model is used in VAST: The bearing is modeled as a flap-lag hinge sequence. A surrogate rotational flap spring and a surrogate rotational lead-lag spring-damper are applied at the respective hinges. A torsion hinge with a discrete surrogate torsional spring is also introduced — it models the elasticity of the control rod and the swashplate.

Equilibrium calculations are conducted in vacuo at nominal rotor speed for blade pitch angles within $[-10°, 20°]$. The elastic tip twist with respect to the FFR is presented in Figure 5 for both implementations of $\mathbf{S}$ used to calculate $\mathbf{Q}_v^f$. At a pitch angle of $10°$, a tip twist of $-0.3°$ is observed with $\mathbf{S} = \mathbf{S}_{\text{tra}}$, while $\mathbf{S} = \mathbf{S}_{\text{tra}} - \tilde{\mathbf{u}}_A \mathbf{S}_{\text{rot}}$ yields a significantly more pronounced tip twist of $-0.5°$. The non-zero tip twist with $\mathbf{S} = \mathbf{S}_{\text{tra}}$ is explained by the complex blade geometry with a pre-twist distribution and a double-swept planform. Accordingly, in contrast to the test case in Figure 3, the pure consideration of centrifugal loads acting on the blade axis introduces some torsion moments in the beam.
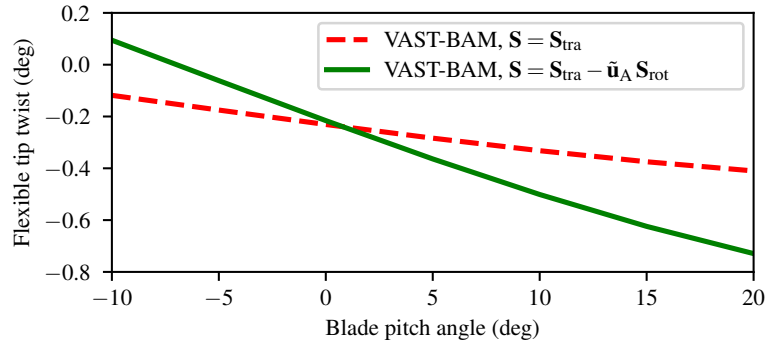

Figure 5. Equilibrium flexible tip twist with respect to the FFR in vacuo at nominal rotor speed for different blade pitch angles

While the results shown in Figure 5 lack reference data for validation, experimental and numerical reference results are available for the Campbell diagram of the prototype blade, which is presented in Figure 6. In [3], the blade eigenfrequencies were identified based on a whirl tower test of the full scale rotor ("reference, experimental"). Furthermore, the eigenfrequencies were calculated with a standalone FE program ("numerical-BAM") using BAM elements (not MBS-capable). The assignment of mode types (L = lead-lag, F = flap, and T/F = torsion/flap) has been adopted from [3].

The bottom of Figure 6 shows the first lead-lag mode ($\times$) and the first flap mode ($+$). These modes feature a negligible deformation of the blade, but primarily contain flap or lead-lag displacements in the respective hinges, so they are rigid body modes. The correlation is very good between all numerical and experimental results. The two different implementations of $\mathbf{S}$ in VAST-BAM do not cause deviations. The same holds for the second flap mode ($+$) which includes flexible flap bending of the blade.

In contrast, differences are observed for the torsion/flap modes ($\bullet$). At a normalized rotor speed of 1.0, the first normalized torsion/flap eigenfrequency T1/F3(a) in the experiment is 4.25. The VAST prediction with $\mathbf{S} = \mathbf{S}_{\text{tra}}$ is 4.11, which is 3 % lower than in the experiment. In contrast, the result using $\mathbf{S} = \mathbf{S}_{\text{tra}} - \tilde{\mathbf{u}}_A \mathbf{S}_{\text{rot}}$ for calculating $\mathbf{Q}_v^f$ is 4.20, which matches the experimental reference with an error of -1 % and also fits the numerical reference better. For the second torsion/flap mode T1/F3(b) with an experimental normalized eigenfrequency of 5.50, the prediction error improves from -5 % to $+1$ %. The improvements are even more significant at higher rotor speeds. The second lead-lag mode ($\times$) is marginally affected by the changed implementation of $\mathbf{S}$. This can be explained by a coupling with the T1/F3(a) mode which has an eigenfrequency very close to that of L2. Through this coupling, the propeller moment — that tends to influence torsion modes — may also affect L2.
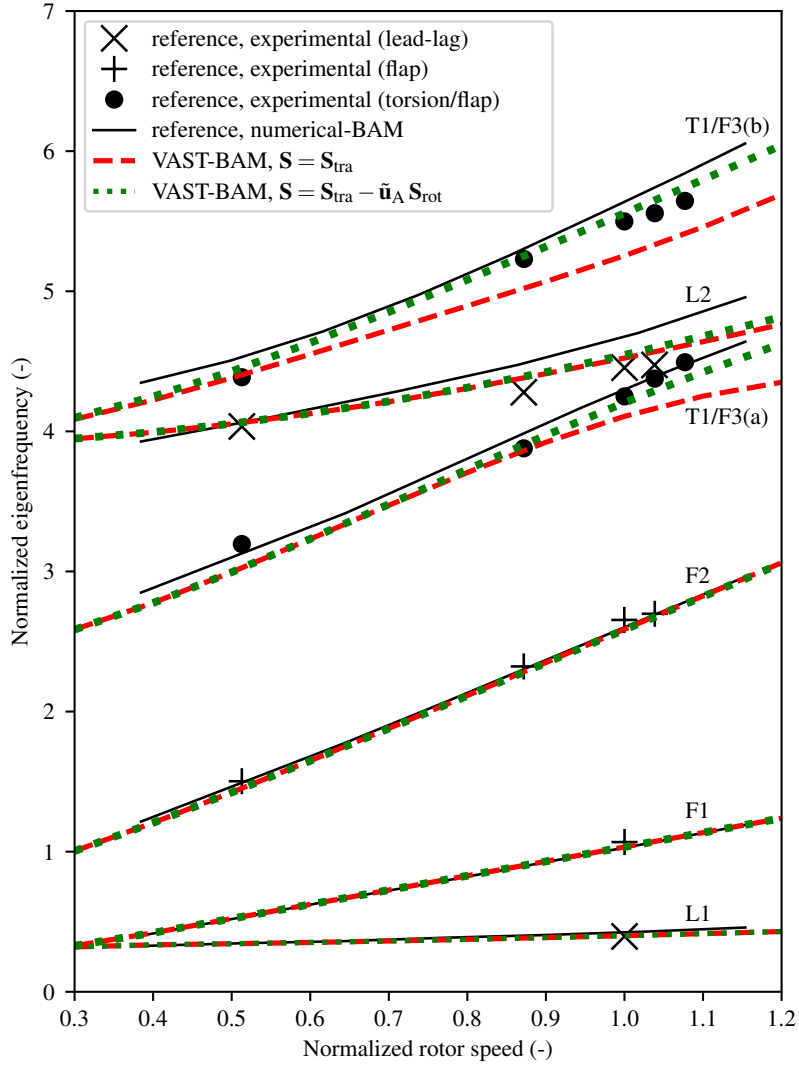
Figure 6. Campbell diagram of a double-swept rotor blade, modeled with the original and complemented shape function matrices $\mathbf{S}$ for the calculation of $\mathbf{Q}_v^f$, reference results taken from [3]

As expected, the upgrade from $\mathbf{S} = \mathbf{S}_{tra}$ to $\mathbf{S} = \mathbf{S}_{tra} - \tilde{\mathbf{u}}_A \mathbf{S}_{rot}$ in the calculation of $\mathbf{Q}_v^f$ primarily affects the torsion modes of the rotor blade. This can be explained by the effect of the propeller moment, as described in section 3.1. The upgrade is needed to properly predict the torsion eigenfrequencies with the FFR formulation implemented for VAST-BAM.

4 CONCLUSIONS

The FFR formulation is used to model helicopter rotor blades as 1D beams within an MBS. To appropriately account for the torsion dynamics of a rotor blade in this approach, rotational shape functions must be considered in the inertia shape integrals and when projecting loads (e.g. centrifugal forces) onto the flexible degrees of freedom. This can be achieved by using the complemented shape function matrix, which includes the effect of rotational deflection combined with the beam axis offset of a particle. The added value of this modified FFR formulation is the consideration of the propeller moment which is demonstrated for an academic test case with analytic reference results. To address a practical test case, a double-swept rotor blade is analyzed. The prediction of the torsion eigenfrequencies significantly improves when using the complemented shape function matrix in the calculation of inertial loads acting on the flexible degrees of freedom.

REFERENCES

[1] Hofmann, J., Weiss, F., Mindt, M.: A New Approach to Comprehensive Rotorcraft Aeromechanics Simulation. In: VFS 77th Annual Forum and Technology Display, Online (May 2021)

[2] Shabana, A.A.: Dynamics of multibody systems. Cambridge University Press, Cambridge (2005)

[3] Skladanek, Y.: Formulation d'un élément fini de poutre pour la dynamique des pales d'hélicoptère de géométrie complexe. PhD thesis, l'Institut National des Sciences Appliquées de Lyon, France (2011)

[4] Skladanek, Y., Cranga, P., Ferraris, G., Jacquet, G., Dufour, R.: A Highly Accurate Beam Finite Element for Curved and Twisted Helicopter Blades. In: ASME 2011 International Design Engineering Technical Conferences and Computers and Information in Engineering Conference, Washington, D.C. (August 2011)

[5] Schiavo, F., Ferretti, G., Vigano, L.: Object-Oriented Modelling and Simulation of Flexible Multibody Thin Beams in Modelica with the Finite Element Method. In: 4th International Modelica Conference, Hamburg, Germany (March 2005)

[6] Weiss, F., Merlis, J., Lojewski, R., Hofmann, J., Roehrig-Zoellner, M.: Rotor Blade Modeling in a Helicopter Multi Body Simulation Based on the Floating Frame of Reference Formulation. In: 48th European Rotorcraft Forum, Winterthur, Switzerland (September 2022)

[7] Johnson, W.: Rotorcraft Aeromechanics. Cambridge University Press, Cambridge (2013)

[8] Bielawa, R.L.: Rotary Wing Structural Dynamics and Aeroelasticity. 2nd edn. American Institute of Aeronautics and Astronautics, Reston, VA (2006)

[9] Houbolt, J.C., Brooks, G.W.: Differential Equations of Motion for Combined Flapwise Bending, Chordwise Bending, and Torsion of Twisted Nonuniform Rotor Blades. NACA TR 1346, Washington, D.C. (1958)